What does a sliding triboelectrical sensor really measure?

Philippe Stempflé, Nicolas Ratier

Highlights

What does a Sliding Triboelectrical Sensor really measure?

Philippe Stempflé, Nicolas Ratier

- Research highlight 1: Sliding Triboelectrical Sensors (S-TENG) belong to the large family of Triboelectric Nanogenerators
- Research highlight 2: Triboelectrical outputs of S-TENGs, modeling single and multi-asperity real contact area, are simulated using LTspice
- Research highlight 3: Triboelectrical behaviors assess instantaneous and averaged velocities of every asperities within the contact area
- Research highlight 4: S-TENGs ultimately probe in real time the tribological behavior of the real contact area during sliding

What does a Sliding Triboelectrical Sensor really measure?

Philippe Stempflé[1,*], Nicolas Ratier[2]

[a]*FEMTO-ST Institute (CNRS), Univ. Bourgogne Franche–Comté (UBFC), Supmicrotech/ENSMM, 26 Chemin de l'épitaphe, CS 51813, 25030, Besançon Cedex, France*

Abstract

For a decade, Triboelectric Nanogenerators (TENG) have been massively developed and optimized either as (i) triboelectric energy harvesters or, (ii) triboelectric self-powered sensors. Unfortunately, it is obvious that the classical tribologists' concerns – like the optimization of both *real* contact area, friction laws and wear processes – have never really been integrated so far neither in their development processes nor in their triboelectrical responses. Thus, a question as basic as "What kind of tribological information can we expect from multi-asperity triboelectric sensor rubbing on a plane in dry friction?" does currently not lead to a trivial answer.

This paper tries to get out this paradoxical situation by simulating triboelectrical behavior of a multi-asperity *real* contact area in dry friction. Results reveal that a sliding triboelectric sensor assesses the *instantaneous* and *averaged* velocities of every interacting asperities within the contact area, finally probing, in real time, the tribological *actual* contact area behavior during sliding.

Keywords: TENG, Self-Powered Sensor, Sliding-TENG, multi-asperity contact, LTspice

*Corresponding author

Email addresses: philippe.stempfle@ens2m.fr (Philippe Stempflé), nicolas.ratier@femto-st.fr (Nicolas Ratier)

[1]orcid:0000-0001-6944-5399

[2]orcid:0000-0003-2447-5118

1. Introduction

When surfaces of two different materials are forced to rub on each other, a finite electrical charge is transfered accross the interface [1, 2, 3]. This phenomenon is known as frictional electrification or tribo-charging [4, 5, 6]. This charge transfer is propagated from occupied high energy states (*valence band*) of the first surface into the inoccupated low energy states (*conductance band*) of the antagonistic surface [7, 4]. This motion is driven by a contact potential difference (CPD), which is proportional to the state densities and energy distributions of the surfaces [8, 9]. Polarity of sliding insulating surfaces is only dependent on the direction of the electrons flow, which itself is linked to the CPD one [10, 11, 12, 8, 5, 13]. A fast and accurate way to assess this CPD is reported using Kelvin probe [14, 9] or Kelvin probe force microscopy [15, 16], for practical purpose.

Until recently, triboelectrical properties of materials have been mainly qualitatively studied in order to identify polarities of rubbing surfaces, leading to the well known *triboelectric series* [17, 12, 13, 18]. Even if a huge improvement has been recently made for optimizing materials in contact, by maximizing their CPD – using materials science [19, 20, 21, 22], for instance – the underlying mechanisms controlling the dynamics of frictional electrification are still partly misunderstood. However, recent works [23, 24, 9, 25, 26] using more quantitative assessments at the nanoscale, have enabled to reveal the existence of, no less than, three mechanisms of transfer – involving electrons [9], ions [27, 28], and matter [24, 23], respectively – simultaneously acting during the triboelectrification process [29]. Although all these mechanisms are quite familiar to tribologists [26, 25], this research field has been remained rather confidential for many years [18, 29].

The revival has been ultimately connected to the recent discovery in 2012 of triboelectric nanogenerators – so-called TENG – by Z.L. Wang's team [30]. By generating charge densities through triboelectrification on surfaces of contacting components moving relative to each other, TENG then drives a current through an external circuit by electrostatic induction, giving the opportunity to use it, either for (i) energy harvesting [31, 32, 33, 34, 35, 36, 37, 38, 39] or directly, (ii) as self-powered sensors [34, 40, 41, 42, 43]. Properties of this current are, indeed, dependent on (i) the relative motion of the charged materials, (ii) their surface charge density and, of course, (iii) their surrounding environment [37, 30], but not on the external circuitry through which the TENG is connected [36]. Knowing these properties, many

designs of TENGs [42, 30] and power management circuitry [44, 45] have been proposed in the literature as many proofs of concept of (i) triboelectrical energy harvesters [46], and/or (ii) self-powered triboelectrical sensors [47].

As a result, TENGs have been deeply world wide studied and developed for a decade, optimizing their mechanical and electrical designs [48, 38, 39, 49, 11, 50] but without any real considerations about tribological aspects and their underlying problematics, as rightly mentioned by Armitage *et al* in their recent papers [35, 36].

Since there is no real way for optimizing any triboelectric generators properties without considering their tribological behaviors in term of: (i) real contact area, (ii) friction laws and (iii) wear behavior, this paper tends to address a first important question. What does a multi-asperity triboelectric sensor really measure when rubbing on a plane in dry friction? Or more precisely, What kind of tribological informations can we expect from this sensor? Answering these questions needs to consider several stages, thus:

(i) a sliding *triboelectrical* model – so-called S-TENG [51, 52, 53, 54] – has been built, as shown in Fig. 1 by combining a single asperity *tribological* model (Fig. 1c) with an *electrical* model (Fig. 1d) in order to simulate the triboelectrical output generated by a single micro-asperity during the sliding process. For this purpose, electrical outputs have been computed using LTspice version 17.0.35 from Analog Devices (`www.analog.com`), which is a powerful free circuit simulator software [55];

(ii) Since the *real* contact area (Fig. 1a) is constituted by multiple micro-asperities (Fig. 1b), a multi-asperity *triboelectrical* sensor has been built, in Fig. 1e, by assembling *elemental* single models in parallel.

Thus, in the following, Section 2 will describe how *triboelectrical* S-TENG models have been built by combining both *tribological* (§2.1) and *electrical* (§2.2) models. Section 3 will then describe results of the triboelectrical simulations: (i) for mono-asperity contact (§3.1) and, (ii) for multi-asperity contacts (§3.2) displaying same and different mechanical properties, respectively. A methodology will be finally proposed for extracting *instantaneous* and *averaged* tribological informations from asperities constituting the *real* contact, leading to figure out what a triboelectrical sensor does measure.

2. Sliding Triboelectrical Sensor modeling

2.1. Tribological models

There are many ways to carried out numerical simulations of tribological behavior [56]. They mainly depend on the complexity of phenomena that are likely to be taken into account as, for instance, the capability to replicate: (i) stiction, (ii) Stribeck effect [57], (iii) stick-slip occurence [58, 59], or (iv) pre-sliding displacement [57]. As shown in Fig. 1c, two tribological models have been built, which differ according to their kinetic conditions.

2.1.1. Model 1

Model 1 (Fig. 1c, top) describes a single *elemental* micro-asperity of polyethylen (PET) coated by a metal electrode, which is forced to rub on a steel plane in dry friction following the classical Coulomb friction model [57]. This micro-asperity is submitted to a sinusoidal motion $x_0(t) = A\sin(\omega t + \varphi)$ with a pulsation ω, a maximum amplitude A and a phase φ. As the two surfaces are moving relatively to each other, the micro-asperity deforms and slides with a dynamics given by the following relationship [60]:

$$m\ddot{x}(t) + k(x - x_0(t)) - \text{sign}(v)\mu_k N = 0 \quad (1)$$
$$\text{(only valid if } A > \frac{\mu_s N}{k}\text{)}$$

with m, the mass of the asperity – depending of its density ρ, its length l, its width w, and its height h; $x(t)$, the *actual* displacement of the asperity versus the steel surface; $x_0(t)$, the *imposed* sinusoidal displacement applied on the asperity's top; k, the shear stiffness of the asperity, which is connected to both its molecular weight [61] and its surface interactions [62]; v, the asperity velocity ; N, the normal load applied on the asperity top; and μ_s and μ_k, the *static* and *kinetic* friction coefficients of the tribological couple, respectively. The averaged values of the latter have been experimentally assessed by using a nanotribometer NTR2 from CSM Instruments, Switzerland [63]. They have been reported in the first column of Table 1 with all parameters used by this model.

Integrations have been solved using a classical Euler-Cromer scheme [60] implemented with GNU OCTAVE [64]. The velocity zero-crossing case has been treated, for the sake of simplicity, by forcing the velocity at zero each time its sign changes [60, 57]. Simulation outputs will provide the friction force *F(t)* and the actual displacement *x(t)* of the *elemental* micro-asperity versus the steel surface.

2.1.2. Model 2

Model 2 (Fig. 1c, bottom) still describes the same metal-coated polyethylen micro-asperity rubbing on a steel plane. However, the latter is now submitted to a continuous velocity v_b driving the micro-asperity in dry friction, as a so-called *mass-on-moving-belt* configuration [65]. Besides, additional parameters will allow us to change the tribological behavior from *sticking* to *gross slip* regimes by controlling the stick-slip occurence during motion [57, 62, 66, 67, 68]. Refering to [69], dynamics of the micro-asperity can be described by the following relationship:

$$\begin{aligned} &m\ddot{x}(t) + c\dot{x}(t) + kx(t) = \\ &N\left[\mu_k + (\mu_s - \mu_k).e^{-c|v_b - \dot{x}(t)|}.\frac{2}{\pi}\text{atan}(s(v_b - \dot{x}(t)))\right] \end{aligned} \tag{2}$$

where, c, is an exponential decay constant; v_b, the steel plane velocity and s, is the sharpness coefficient of the $2/\pi$.atan(.) function, which here is used to represent the friction force transition along zero relative velocity. It avoids us to treat any velocity zero-crossing condition, as carried out in Model 1. All the other parameters are similar to those of the Model 1 and are reported in the second column of Table 1.

Owing to the non-linear behavior of Eq. 2, dynamical system has been computed using Runge-Kutta integration method – so-called ODE45 for *explicit variable step Runge-Kutta fourth and fifth-order method* [70] – included within GNU OCTAVE [64].

It is worth noting that although both tribological simulations are likely to provide the friction force $F(t)$ and the *actual* displacement of the *elemental* micro-asperity $x(t)$ versus the steel surface, only the latter will be essential for building the triboelectrical model, as explained in the next section.

2.2. Triboelectrical model

Only the *actual* displacement of the *elemental* micro-asperity versus steel surface, *x(t)*, is indeed needful to feed the present triboelectrical model because its value is directly dependent on any sticking or slipping events (and even any local wear process) felt by the micro-asperity [62, 71]. The latter – by means of its *actual* displacement *x(t)* – thus appears as a very sensitive probe providing every local tribological informations occuring in real time at the asperity's scale.

Parameters	Model 1	Model 2
Dimensions of PET micro-asperity (length×width×height) [µm]	10×10×110	10×10×110
Mass of PET micro-asperity m [kg]	10^{-12}	10^{-12}
Shear stiffness of PET micro-asperity k [N/m] [61]	10 – 155	25 – 155
Maximum amplitude of PET micro-asperity [µm]	9	-
Normal load applied on PET micro-asperity N [N]	10^{-3}	10^{-3}
Static friction coefficient μ_s between PET/Steel	0.28	0.28
Kinetic friction coefficient μ_k between PET/Steel	0.22	0.22
Exponential decay constant c [57]	-	10^{-7}
Drive steel plane velocity [m/s]	0	1 – 10

Table 1: Mechanical and tribological parameters of tribological models: Model 1 computes the tribological behavior of a metal-coated polyethylen micro-asperity rubbing on a steel plate with an alternative sinusoidal motion; its movement is described by Eq. (1); Model 2 computes the tribological behavior of the same micro-asperity submitted to a constant drive steel plane velocity v_b; its movement is described by Eq. (2).

Keeping these considerations in mind, *x(t)* can then be the unique input of our electrical circuit modelling the triboelectrical behavior of an *elemental* tribocontact, as shown in Fig. 1d. The developement of the latter can be split in several stages:

- First stage, an *elemental* triboelectrical model is built from the description of the macroscopic TENG's equivalent circuit model proposed by Niu *et al.* [39]. In the latter the whole equivalent circuit is basically represented by a serial connection of an ideal voltage source (V_{TENG}) – originated from the separation of the polarized tribo-charges [25]– and, a capacitor (C_{TENG}) due to the capacitance between the two electrodes [30]. Equation governing the electrical behavior of this TENG is given by [39]:

$$V = -\frac{1}{C_{\mathrm{TENG}}} Q + V_{\mathrm{TENG}} \tag{3}$$

  where, the values of the ideal voltage source (V_{TENG}) and the capacitance (C_{TENG}) need to be specified. For complex geometry, $V_{\mathrm{TENG}}(x)$ and $C_{\mathrm{TENG}}(x)$ relationships can be obtained by solving electrostatics equations for discrete values of x with a numerical method as finite

element analysis, and interpolation to get an approximated continuous formulation [52]. However, for a single *elemental* squared asperity sliding on a plane, the following relationships can be derivated [39]:

$$V_{\mathrm{TENG}}(x) = \frac{\sigma d_0 x}{\varepsilon_0 (l - x)} \tag{4}$$

$$C_{\mathrm{TENG}}(x) = \frac{\varepsilon_0 w (l - x)}{d_0} \tag{5}$$

with, σ, the tribo-charge surface density [11, 6], linked to the initial triboelectrical charges Q_0 [12], which can be assessed using Kelvin Probe [14] or Kelvin Probe Force Microscopy (KPFM) [15]; d_0, the effective dielectric thickness, ε_0, the vacuum permittivity ($\varepsilon_0 = 8.8541878 \times 10^{-12}$ F/m), l and w, are respectively the length and width of the dielectrics, and x(t), the *actual* displacement controlled by the frictional behavior, which is computed by the tribological models detailed in section 2.1. All triboelectric parameters are reported in Table 2.

According to the basic electrodynamics theory [7, 1], and as shown in Eq. (4) and (5), only the *actual* displacement $x(t)$ and the structural parameters do influence on V_{TENG} and C_{TENG} relationships. Motion parameters, such as velocity and acceleration, do not act explicitely [39].

- Second stage, knowing the $V_{\mathrm{TENG}}(x)$ and $C_{\mathrm{TENG}}(x)$ relationships, the elemental triboelectrical behavior of the S-TENG can be then implemented as a user's component into LTspice software [55], as shown in Fig. 1d. Implementation details of this subcircuit are reported in the appendix. This S-TENG can thus be connected to any electronic component or commercial microchip already embedded within the LTspice library in order to simulate complex electrical response, as power management circuit [44, 45], for instance. However, in spite of its extensive components library, LTspice is mainly chosen here owing to its peculiar ability to manage highly non-linear equations [55, 72]. Thus, after inserting other circuit elements – as load resistors or storage capacitors – and specifying the *actual* displacement *x(t)* computed by the previous tribological models, LTspice is able to assess the voltage and current outputs of the S-TENG component generated by triboelectric effect.

This electrical outputs will, of course, depend on the contact and tribological conditions – *ie*, shear stiffness k, and μ_k/μ_s ratio, and damping coefficient c, and so on – included within the tribological models.

- Third stage, a multi-asperity contact can then be efficiently modeled by assembling many *elemental* S-TENG components in parallel, leading to an *in-situ* tribological sensor detecting events occuring within a *real* contact area, as pictured in Fig. 1e. It is worth noting that this discrete approach assumes no interaction between micro-asperities. This is well suited in our case owing to the low applied normal load N (cf. Table 1) leading to a low contact density A_r/A_0. According to Goryacheva [73], there is a good agreement between theory and experiment using a discrete approach with these loading conditions.

Parameters	Values
Relative permitivity and thickness of PET [µm]	ε_{r_1}=2.2 – $d_1 = h = 110$
Relative permitivity and thickness of Steel [µm]	Conductor – $d_2 = 0$
Effective dielectric thickness ($d_0 = \frac{d_1}{\varepsilon_{r_1}} + \frac{d_2}{\varepsilon_{r_2}}$) [µm]	50
Dielectric length l [µm]	10
Dielectric width w [µm]	10
Tribocharge surface density σ [$\mu C/m^2$]	80

Table 2: Parameters of the *elemental* triboelectric LTspice model. Materials constants are extracted from [74, 20, 17, 75].

3. Results and discussion

3.1. Single micro-asperity triboelectrical behaviors in dry friction

3.1.1. Tribological behavior of a single micro-asperity

Both tribological and triboelectrical behaviors of a squared micro-asperity of metal-coated polyethylen, rubbing on a steel plane, are simulated and plotted in Fig. 2 for two shear stiffness values. As aformentionned varying asperity shear stiffness k is a good way to take into account any changes of (i) molecular weight of polyethylen [61] or (ii) interface properties [62, 76] in our tribological simulations. Model 1 in Fig. 2a is used and parameterized with values reported in Table 1.

Figure 2c and 2d plot the evolution of the friction force $F(t)$ versus time for asperity's stiffness of 10 N/m and 155 N/m, respectively. Whatever the stiffness value, the friction force *F(t)* displays a classical sawtooth behavior showing oscillations due to the gap between μ_k and μ_s, which confirm stick-slip occurences [77, 78]. While the force level only depends on friction coefficients, its oscillation amplitude and frequency are both stiffness dependent, as clearly shown in Fig. 2c with respect to Fig. 2d, keeping the same μ_k/μ_s ratio [79].

More interesting are results plotted in Fig. 2e and 2f showing the *imposed* $x_0(t)$ and *actual* displacements $x(t)$ *vs.* time of the asperity displaying stiffness of 10 N/m and 155 N/m, respectively. Whatever the stiffness level, the micro-asperity moves in slips following the *imposed* motion $x_0(t)$ but sticks and slips as it moves along. However, while both displacements are quite similar and synchronized for the highest stiffness (Fig. 2f), a *stairstep* displacement is clearly observed for the *actual* displacement $x(t)$ when the stiffness is low enough (Fig 2e). As expected, the lower the shear stiffness k the longer the delay between the *imposed* and the *actual* displacements, which finally causes a smaller displacement amplitude during the sliding phase than the imposed one by $x_0(t)$ – see Fig. 2e. Thus, this *stairstep* motion appears to be clearly connected to stick-slip occurrences induced by the tribological behavior, shown in Fig. 2c and 2d. These results strengthen our assumption that all tribological informations are embedded within the *actual* displacement $x(t)$ without any need to assess to the friction forces.

3.1.2. Triboelectrical behavior of a single micro-asperity

Since the *actual* displacement *x(t)* embeds all frictional changes occuring within the tribocontact, its evolution with time is then used as input to feed the triboelectrical model S-TENG, described in Fig. 1d and in appendix. Let us recall that this model computes electrical signals generated when a metal-coated polyethylen micro-asperity is rubbing on a steel plane following the tribological Model 1 [25, 23]. For this purpose, the *elemental* triboelectrical LTspice component is then connected to a resistor of 1 MΩ in order to compute both the current $i(t)$ through the resistor and the voltage $V(t)$ across it, as shown in Fig.2b.

Variations of the voltage outputs with time are plotted in Fig. 2g and 2h. They correspond to tribological simulations carried out for stiffness of 10 N/m and 155 N/m, respectively. Owing to the size of the rubbing micro-asperity, voltage levels appear of course very low – around several hundred

µV – but, these values should greatly raise by considering all the micro-asperities, which are likely to slide within a macroscopic real contact area. Besides, it is worth noting that the voltage outputs look like a comb signal whatever the stiffness value.

In order to figure out the meaning of this signal, Fig. 3a superimposes on the same graph the output voltage $V(t)$ plotted in Fig 2g and the corresponding *actual* displacement $x(t)$, plotted in Fig 2e. As a result, it appears that electric voltage is only observed each time the asperity slides while no voltage is detected during the sticking period. Besides, voltage peaks perfectly match to every state changes occuring of the *actual* displacement. So, what does this triboelectrical signal really mean?

Trying to answer this question, the *imposed* sinusoidal displacement $x_0(t)$ is now injected instead of the *actual* displacement $x(t)$ as input of the S-TENG triboelectrical component. The voltage output $V(t)$ and the *imposed* displacement $x_0(t)$ are then both plotted in Fig. 3c. After a sudden jump connected to the initial transcient period, *V(t)* also displays a sinusoidal behavior, which is out of phase versus the input signal $x_0(t)$. Since this phase difference is exactly $\pi/2$, the output voltage *V(t)* clearly appears as the derivative function of the input and so, the *asperity velocity*. Let us noting that these results are perfectly inline with the experimental ones, recently published by Armitage *et al* [35], showing that TENG's output is proportional to the imposed velocity.

Keeping this consideration in mind, the comb signal plotted in Fig. 3a can then be analyzed more carefully. Indeed the zero-voltage of *V(t)* output between each peak corresponds to the zero-crossing state of the velocity, which has been treated in the Model 1, just by forcing the velocity at zero, each time its sign changes. Besides, peaks' amplitudes in Fig. 3a do not mean anything in this case as they only result from the derivative of discontinuous functions. In contrast, time-gaps between each peaks do make physical sense, because they assess sticking time of the asperity between two slip events. Nevertheless, in a more general case, as the one presented in section 3.2, informations about individual velocities of each asperity will be able to be extracted from voltage signals by considering tribological Model 2 in a multi-asperity contact. Thus, triboelectrical voltage provides information about the *relative* velocity at the scale of the asperity which, of course, is different to the *imposed* sliding velocity owing to friction. It is worth noting that Niu et al have proposed in [39] an analytical relationship linking triboelectrical voltage to sliding velocity. However, their relationship – only valid

at constant velocity – is unable to measure any relative velocity variations and so, frictional dissipation assessment. On the contrary, our relationship linking triboelectrical voltage to *actual* relative velocity gives the opportunity to assess frictional dissipation via asperities' velocity variations. Hence, in the framework of self-powered sensors, it seems that a triboelectrical signal, as shown in Fig. 3a, could be used for accurately probing the various events occuring, at the microscale, within the *real* contact area.

Integrating now the electric current flowing out the S-TENG component – by means of the classical relationship $Q(t) = \int_0^t i(\tau)d\tau + Q_0$ with, Q_0, the initial charge, which is connected to the tribocharge surface density σ – the evolution of the corresponding triboelectrical charge *vs.* time can be assessed and plotted in Fig. 3b.

As expected, the latter strongly increases with time during the sliding period, while it rather stays constant during the sticking period – the slightly increase, observed in Fig. 3b, is actually only due to the time constant for charging the surface capacitance. Again, charge values are very low here considering only one micro-asperity, but will strongly increase later when considering a multi-asperity contact in section 3.2. Hence, in the framework of energy harvesting, this result clearly means that the best charging process is the one obtained when no stick-slip occurs [80], because the latter clearly induces a strong decrease of the charge slope, as shown in Fig. 3b.

In order to get further and trying to figure out what really happen within a multi-asperity contact area, *multiple* micro-asperity triboelectrical behavior has been simulated by assembling many *elemental* triboelectrical S-TENG components in parallel, leading to an *in-situ* tribological sensor detecting events occuring within a *real* contact area.

3.2. Multiple micro-asperity triboelectrical behaviors in dry friction

As reminded in Fig. 4a, a *real* contact area is now constituted by numerous single micro-asperities in interaction during the sliding motion. Four *elemental* S-TENG modules have thus been connected in parallel in order to simulate triboelectrical output generated by four rubbing micro-asperities (Fig. 4b).

3.2.1. Asperities with same properties submitted to tribological Model 1

At first, all these modules are supposed identical assuming that every *elemental* asperities have the same dimensions (10 µm × 10 µm) and the same stiffnesses (75 N/m). In the same time, triboelectrical behavior of

a single asperity, displaying the same contact area as the whole *elemental* asperities, has been tested too for the sake of comparison (Fig. 4d).

Results of these simulations, plotted in Fig. 4c, clearly show that triboelectrical behaviors are not the same by considering four interacting asperities (blue peaks) and a single one displaying the same contact area (red peaks): (i) the output voltage coming from the whole four micro-asperity is greatly higher and, (ii) the two signals are clearly out of phase because *stick* and *slip* events do not occur at the same time during the both simulations.

These results prove that a *real* contact area can only be simulated by taking into account *all* the interacting asperities within it (or at least a statistically representative amount) [73]. Indeed, Fig. 4c shows that the triboelectrical output signal combines all the elemental voltages coming from each *stick* and *slip* events. Thus, every tribological events, plotted in blue appear in phase because all asperity display the same shear stiffness. What does it happen if each asperity has its own one?

3.2.2. Asperities with different properties submitted to tribological Model 1

Figure 5 plots triboelectrical simulations of a *real* contact area constituted of four micro-asperities modelled by four S-TENG wired in parallel, where each asperity now displays specific stiffness ranked from 25 N/m to 155 N/m. Each asperity still follows the tribological Model 1. Output currents are now studied instead of output voltage in order to extract the individual behavior of each asperity. Indeed, in a parallel circuit, the current split amoung each component but the voltage remains the same.

Thus, all electric current outputs can be simultaneously plotted in Fig. 5a, for each asperity, with a different color. It is worth noting that LTspice considers as positive an incoming current into a subcircuit, explaining why outputs are now reversed versus the voltage ones, plotted until now. Since each asperity has its own stiffness all signals are clearly out of phase, revealing asynchronous *stick* and *slip* events, in contrast to what has been observed in Fig. 4c.

Let us mention that same kind of response can be obtained in Fig. 5b by keeping constant the stiffness of micro-asperities and intentionally dephasing all input signals (by changing φ in the sinusoidal motion). This confirms, if needed, that out-of-phase output signals shown in Fig. 5a well comes from local changes of tribological behaviors at the micro-asperity scale [71].

3.2.3. Asperities with different properties submitted to tribological Model 2

In order to study the triboelectrical behavior of multi-asperity contact in a more general case, same simulations – involving four micro-asperities displaying specific stiffnesses – have been carried out using the tribological Model 2 (See Fig. 6a and 6b). Shear stiffnesses are 25, 50, 100 and 155 N/m, respectively. Simulation parameters are those reported in Table 1.

Figure 6c plots the output voltage for a drive plane velocity set at 1 m/s. Let us recall that this signal is, in fact, the combined velocity of the four asperities and so, the one of the multi-asperity *real* contact area. Thus, Fig. 6c reveals that – owing to the suffered tribological conditions and despite the constant drive plane velocity – this *real* contact area tends to quickly stop because its own velocity strongly drops.

By changing the drive plane velocity from 1 m/s to 10 m/s, keeping constant all other parameters, Fig. 6d reveals that, this time, the real contact area is well driven by friction – with a very low damping – along the steel plane. This damping is of course closely linked to both the exponential decay constant c, and the friction coefficients couple set in the model (cf. Table 1). As a result, the average velocity of the multi-asperity real contact area, plotted in Fig. 6d, oscillates uniformly with time.

Integrating now the electric current flowing out the S-TENG component, the evolution of the triboelectrical charge *vs.* time can be assessed and plotted in Fig. 6g. This triboelectric charge continuously increases with sliding time. However, considering now a multi-asperity contact, constituted of four asperities, charge values have been increased by a factor 2000 with respect to the ones involving only one micro-asperity (plotted in Fig. 3b). This results is of great interest in the framework of energy harvesting, for optimizing the design of triboelectric nanogenerators TENG.

Since triboelectrical outputs plotted in Fig. 6c and 6d are rather complex signals embedding tribological behaviors of several asperities, could it be possible to extract elemental behavior of each asperity?

3.2.4. Average behavior of individual asperity within a real contact area

Applying Fast Fourier Transform (FFT) on these output voltages (Fig. 6c and 6d) seems to be a promising way for extracting the *elemental* behaviors of the *real* contact area components, as shown in Fig. 6e and 6f, respectively. Let us recall that the FFT sums samples in the original units (ie, V) multiplied by unitless complex values due to discretization [81]. So, units after FFT remain the same as the original signal.

As a result, FFT signals reveal four different frequencies, which are quite independent of the drive plane velocity, since all are observed in the both figures. Their number corresponds to the one of asperities involved within the contact, and their frequencies seem closely linked to their stiffness (similar for the both cases too). Therefore, one can rationally assume that each frequency could be related to a specific asperity sliding at its own velocity.

To check this assumption out, let us plot in Fig. 7a and 7b, the FFT of the electric currents flowing out each *elemental* triboelectrical component for the both drive plane velocities. Again, currents are plotted here instead of voltage to enable to label each frequency with its own triboelectrical component, which itself is associated to a specific asperity. Hence, Fig. 7a and 7b give same informations as the ones plotted in Fig. 6e and 6f, owing to linear relationship between current and voltage for resistor.

They however both confirm that each frequency well corresponds to a specific asperity, whatever the drive plane velocity. There is therefore a specific frequency for each asperity, itself connected with all involved interfacial properties [62, 71], especially the shear stiffness here. As shown in Fig. 7a and 7b, the greater the asperity's stiffness the higher the frequency.

In contrast to their positions, frequency peaks amplitudes are clearly velocity-dependent as reported in Fig. 7a and 7b. According to the physical meanings of the Fourier's component amplitudes [82], they should be linked here to the *actual* average velocity amplitude of each asperity during simulations. Thus, for each asperity, the higher the amplitude of its *average* velocity the greater the corresponding FFT peak.

Herein, Fig. 7a and 7b well show the influence of the drive plane velocity on the *average* velocity amplitude of each asperity according to their local stiffnesses, thus:

- for the lowest one – i.e. 1 m/s – the average velocity amplitudes of all the four asperities are quite similar before to get at rest, although they display different stiffnesses (Fig. 7a). Thus, at low drive plane velocity, asperities seem all moving in the same overall motion and then gradually decrease their average velocity, all together, until the complete stop.

- In contrast, for a steady state sliding occuring at the highest drive plane velocity – 10 m/s – each asperity moves at its own velocity amplitude (Fig. 7b) in connection with its stiffness. The lower the shear stiffness

the higher the average velocity amplitude because sticking process does have time to settle down, forcing the micro-asperity to follow the drive plane motion.

Therefore, the Fast Fourier Transform appears to be a good tool for analyzing tribological properties occuring at the asperity scale in the framework of self-powered triboelectrical sensors. Applied to triboelectrical outputs, FFT is indeed likely to analyse the sliding *real* contact area in order to extract: (i) the number of asperities sliding or sticking; (ii) their average velocity, (iii) their shear stiffnesses, and more generally, (iv) any changes in tribological conditions – ie, friction or damping, surface energy, or any wear process. However, FFT analysis is well suitable for permanent regimes [82], that is, when triboelectrical signals stay stable and do not change much with time. But tribological contacts can seldom be considered as permament regimes; they rather look like a succession of transient events. Hence, this kind of analysis could be impoved if the FFT could be able to be carried out in *real time*, or at least, with a computational time much lower than caracteristic times of aformentioned tribological phenomena.

3.2.5. Real-time behavior of individual asperity within a real contact area

A way to adress this problem is to use a *Short-Time Fourier Transform* (STFT), which is a classical Time-Frequency tool [81]. Basically, this transform realize a FFT in *real time* on a transient signal using a *temporal sliding window* [83]. The width of this *sliding window* is generally chosen to fit to the characteristic time of the studied phenomenon. For real time rubbing analysis it should be very short but, of course, can be increased when considering much longer tribological phenomena, as wear processes for instance.

In order to check this assumption out, Short-Time Fourier Transforms are carried out on triboelectrical signals – seen in Fig. 6c and 6d – using a Time-frequency Toolbox library running on GNU OCTAVE, and freely available online at `http://tftb.nongnu.org/`. Short-time FFT is evaluated using the integrated `tfrstft` function leading to the corresponding spectrograms plotted in 2D (Fig 8a and 8b) and 3D (Fig 8c and 8d), respectively. Normalized frequencies are used here for the sake of comparison. As a result, frequencies variations can now be studied *vs.* time, and so, their tribological interpretations too.

Refering to our previous FFT analysis, the both signals plot the evolution of the velocity of the real contact *vs.* time, when the drive plane velocity

varies from 1 m/s to 10 m/s, respectively. The aformentioned four frequency peaks are clearly retrieved in Fig. 8 if one forgets the highest frequencies corresponding to harmonics of fundamental ones.

What is really new on these spectrograms is that the amplitude and frequency of each peak both evolve with time, revealing tribological changes within the rubbing contact area. Indeed, by assuming that friction law varies very little within the *sliding window*, variations of frequencies amplitude can therefore be interpreted as *real time* tribological modifications at the asperities'scale. This is because individual shear stiffness of each asperity is not only defined by its bulk properties but also by its interface properties which can evolved versus time [71, 24], thus:

- When drive plane velocity is high enough (10 m/s), the real contact area appears quite constant versus time (Fig. 8b and 8d), all the four asperities continuously slide with some velocity fluctuations along the path because some local stick-slip events;

- In contrast when drive plane velocity is decreased at 1 m/s, asperities evolve independently of each other, as shown in Fig. 8a and 8c. Some keep sliding while other stop suddenly during a period depending on their own shear stiffness, then restart sliding to finally get at rest owing to the damping process.

As a result, the spectrogram finally maps the evolution of the *real* contact area with respect of time.

As mentioned earlier, owing to the low applied load, asperities have been considered up to now as independent – ie, without any relationship between them. It would be interesting to wonder about the effect of possible interactions of neighboring asperities on triboelectrical voltage in the case of an experimental triboelectrical sensor. Indeed, since the latter will essentially probe the relative velocity of each asperity, which itself is connected to its contact stiffness, interaction of neighboring asperities – during wear processes or at high applied load, for instance – will basically lead to assess an equivalent contact stiffness taking into account all the interacting asperities. Thus, in a real tribological conditions, when asperities suffer wear for instance, a triboelectrical sensor will probably not be able to sense each asperity independently but rather the interactions between them via some progressive changes of contact stiffness at the asperity scale. Since wear process leads

to change interactions between asperities, a real experimental self-powered triboelectrical sensor will then likely to be an interesting in-situ wear sensor too.

4. Conclusion

The goal of this paper was to understand what kind of tribological informations could be expected from a sliding triboelectrical sensor (S-TENG). For this purpose,

- a sliding triboelectrical model has been first built by combining a single asperity *tribological* model with an *electrical* model in order to simulate – using LTspice – the triboelectrical output generated by a single micro-asperity during the sliding process. Results have showed that the latter actually corresponds to the *elemental* asperity velocity;

- a multi-asperity triboelectrical sensor has been then built by assembling elemental single triboelectrical models in parallel modelling a *real* contact area constituted by multiple asperities. Results have revealed that the voltage output gives then the *average* velocity of the *real* contact area. Applying the Fast Fourier Transform on this output has enabled to extract: (i) the number of asperities sliding or sticking; (ii) their average velocity, (iii) their shear stiffnesses, and (iv) any changes in tribological conditions. Applying a Short-Time Fourier Transform on the same signal has provided, in addition, *real time* tribological modifications at the asperities'scale.

Thus, a sliding triboelectrical sensor clearly assesses the *instantaneous* and *averaged* velocities of every interacting asperities within the contact area to finally probes in *real time*, the *actual* contact area behavior during sliding.

Appendix

This appendix describes how the *elemental* triboelectrical component is built, tested and implemented in the circuit simulator software LTspice Version 17.0.35 (`www.analog.com`).

To simulate the behavior of a triboelectric generator in sliding mode an electrical model is composed of a voltage source V_{TENG} and a capacitor C_{TENG} placed in serial connection [39]. The voltage and the capacitance are defined

by Eq. 6 and Eq. 7, respectively. Both depend on the distance x which is the *actual* elemental displacement.

$$V_{\mathrm{TENG}}(x) = \frac{\sigma d_0 x}{\varepsilon_0 (l - x)} \tag{6}$$

$$C_{\mathrm{TENG}}(x) = \frac{\varepsilon_0 w (l - x)}{d_0} \tag{7}$$

A first implementation of this model in LTspice is proposed as follow:

The voltage generator V_{TENG} can be modelized by an arbitrary behavior voltage source (Spice component B). The capacitor C_{TENG} can be defined by a charge model definition of a capacitance. The equivalent circuit is shown in Fig. 9.

Simulation of this circuit has been compared with the analytic result given by Eq. 4 with data Table 1 in [39], $\sigma = 100.0\ \mu C/m^2$, $d_0 = 31.25\ \mu m$, $w = 0.05\ m$, $l = 0.08\ m$, $x(t) = vt$ with $v = 1\ m/s$. The circuit is finally loaded with a resistive charge of $1G\Omega$. As a result, simulation gives an absolute relative error at $t = 0.05\ s$ of 7×10^{-3}.

A more accurate circuit is now proposed for C_{TENG}. This second model of S-TENG is shown in Fig. 10. The component with index `v` modelizes the voltage equation (6) and the components with indexes `c` modelize the capacitance equation (7). Comparison of its output with the analytical equation is now 1×10^{-6} at $t = 0.05\ s$.

In order to simulate multiple *elemental* micro–asperities, the second model is now grouped as a macro-component represented by the symbol shown in Fig. 11. The parameters σ, d_0, w and l, as well as the distance x, are those of equations (6) and (7). They are expressed in international system unit but given as voltages inside LTspice. The load must be connected between terminals V+ and V-.

The definition of the macro-model is simply the Spice description of the circuit shown on Fig. 10. It must be, for instance, written in a file `nanotribogen.sub`. Simulation command `.lib nanotribogen.sub` must be added inside LTspice to use it, so LTspice knows what really represents the symbol of the macro-component.

```
.subckt s-teng x sigma d0 w l V+ V-
Rx x 0 10G
Bv N003 V- V=V(sigma)*V(d0)*V(x)/{epsilon0}/(V(l)-V(x))
```

```
Fc V+ N003 Vc 1
Bc N001 0 V={epsilon0}*V(w)*(V(l)-V(x))/V(d0)*(V(V+)-V(N003))
Vc N001 N002 0V
Cc N002 0 1
.param epsilon0=8.8541878e-12
.end s-teng
```

LTspice outputs of each S-TENG model are shown in Fig. 12 and compared to results from analytical equations. The three curves corresponding to: (i) the analytical expression, (ii) the second model, and (iii) the macro-component are clearly superimposed. In contrast, the first model gives a curve a little above the others.

Acknowledgments

Authors thank Jean-Michel Friedt from FEMTO-ST to point out the Time-frequency Toolbox library running on GNU OCTAVE and for our fruitful discussions about Time-frequency assessments.

References

[1] W. R. Harper, Contact and Frictional Electrification, OXFORD University Press, 1967.

[2] F. A. Vick, Theory of contact electrification, Br. J. Appl. Phys. 4 4 (S1) (1953).

[3] W. D. Greason, Investigation of a test methodology for triboelectrification, Journal of Electrostatics 49 (2000) 245–256.

[4] S. Pan, Z. Zhang, Fundamental theories and basic principles of triboelectric effect: A review, Friction 7, 2–17 (2019). https://doi.org/10.1007/s40544-018-0217-7.

[5] K. Nakayama, Tribocharging and friction in insulators in ambiant air, Wear 194 (1996) 185–189.

[6] Y. Zhang, T. Shao, A method of charge measurement for contact electrification, Journal of Electrostatics 71 (2013) 712–716.

[7] M. Willatzen, Z. L. Wang, Theory of contact electrification: Optical transitions in two-level systems, Nano Energy 52 (2018) 517–523.

[8] S. Kim, Modeling of tribo-charge density using a transition matrix element in a teng system: Approximate calculation, Results in Physics 12 (2019) 1417–1420.

[9] F. Galembeck, T. A. L. Burgo, Chemical Electrostatics - New Ideas on Electrostatic Charging: Mechanisms and Consequences, doi 10.1007/978-3-319-52374-3 Edition, Springer International Publishing AG, 2017.

[10] V. Albrecht, A. Janke, E. Németh, S. Spange, G. Schubert, F. Simon, Some aspects of the polymers' electrostatic charging effects, Journal of Electrostatics 67 (2009) 7–11.

[11] C. Zhang, L. Zhou, P. Cheng, X. Yin, D. Liu, X. Li, H. Guo, Z. L. Wang, J. Wang, Surface charge density of triboelectric nanogenerators: Theoretical boundary and optimization methodology, Applied Materials Today 18 (2020) 100496.

[12] D. M. Gooding, G. K. Kaufman, Tribocharging and the triboelectric series, in: Encyclopedia of Inorganic and Bioinorganic Chemistry, John Wiley & Sons, Ltd., 2019, p. DOI 10.1002/9781119951438.eibc2239.pub2.

[13] H. Zou, Y. Zhang, L. Guo, P. Wang, X. He, G. Dai, H. Zheng, C. Chen, A. Chi Wang, C. Xu, Z. L. Wang, Quantifying the triboelectric series, Nature Communications 10:1427 (2019).

[14] A. Subrahmanyam, C. Suresh Kumar, Kelvin Probe for Surface Engineering, Ane Books Pvt Ltd, 2009.

[15] H. O. Jacobs, H. F. Knapp, A. Stemmer, Practical aspects of kelvin probe force microscopy, Rev. Sci. Instrum. 70 (3) (1999).

[16] S. Sadewasser, T. Glatzel (Eds.), Kelvin Probe Force Microscopy - From Single Charge Detection to Device Characterization, Springer Series in Surface Sciences, 2018.

[17] A. F. Diaz, R. M. Felix-Navarro, A semi-quantitative tribo-electric series for polymeric materials: the influence of chemical structure and properties, Journal of Electrostatics 62 (2004) 277–290.

[18] T. A. L. Burgo, F. Galembeck, G. H. Pollack, Where is water in the triboelectric series?, Journal of Electrostatics 80 (2016) 30–33.

[19] A. Chen, C. Zhang, G. Zhu, Z. L. Wang, Polymer materials for high-performance triboelectric nanogenerators, Advanced Science 7 (14) (2020) 2000186.

[20] I. Shinohara, F. Yamamoto, H. Anzai, S. Endo, Chemical structure and electrostatic properties of polymers, Journal of Electrostatics 2 (1976) 99–110.

[21] N. K. Myshkin, M. I. Petrokovets, A. V. Kovalev, Tribology of polymers: Adhesion, friction, wear, and mass-transfer, Tribology International 38 (2005) 910–921.

[22] Z. Zhao, L. Zhou, S. Li, D. Liu, Y. Li, Y. Gao, Y. Liu, Y. Dai, J. Wang, Z. L. Wang, Selection rules of triboelectric materials for direct-current triboelectric nanogenerator, Nature Communications 12:4686 (2021) https://doi.org/10.1038/s41467–021–25046–z.

[23] H. T. Baytekin, A. Z. Patashinski, M. Branicki, B. Baytekin, S. Soh, B. A. Grzybowski, The mosaic of surface charge in contact electrification, Science 333 (15 July 2011) 308–311.

[24] J. A. Wiles, M. Fialkowski, M. R. Radowski, G. Whitesides, B. A. Grzybowski, Effects of surface modification and moisture on the rates of charge transfer between metals and organic materials, J. Phys. Chem. B 108 (2004) 20296–20302.

[25] T. A. L. Burgo, A. Erdemir, Bipolar tribocharging signal during friction force fluctuations at metal–insulator interfaces, Angew. Chem. Int. Ed. 53 (2014) 12101 –12105.

[26] T. A. L. Burgo, C. A. Silva, L. B. S. Balestrin, F. Galembeck, Friction coefficient dependence on electrostatic tribocharging, Scientific Reports 3 (2384) (2013) DOI: 10.1038/srep02384.

[27] T. A. L. Burgo, T. R. D. Ducati, K. R. Francisco, K. J. Clinckspoor, F. Galembeck, S. E. Galembeck, Triboelectricity: Macroscopic charge patterns formed by self arraying ions on polymer surfaces, Langmuir 28 (2012) 7407–7416.

[28] L. S. Mc. Carty, G. M. Whitesides, Electrostatic charging due to separation of ions at interfaces: Contact electrification of ionic electrets, Angew. Chem. Int. Ed. 47 (2008) 2188 – 2207.

[29] S. W. Thomas III, S. J. Vella, M. D. Dickey, G. K. Kaufman, G. M. Whitesides, Controlling the kinetics of contact electrification with patterned surfaces, J. AM. CHEM. SOC. 131 (2009) 8746–8747.

[30] Z. L. Wang, L. Lin, J. Chen, S. Niu, Y. Zi, Triboelectric Nanogenerators, doi 10.1007/978-3-319-40039-6 Edition, Springer International Publishing Switzerland, 2016.

[31] J. Hu, P. Gu, X. Zeng, Q. Zhou, C. Liang, D. Liu, X. Chen, Triboelectric charging behavior of a rough surface sliding on a flat plane, Journal of Electrostatics 97 (2019) 85–94.

[32] C. Wu, A. C. Wang, W. Ding, H. Guo, Z. L. Wang, Triboelectric nanogenerator: A foundation of the energy for the new era, Adv. Energy Mater. 9 (1) (2018) 1802906.

[33] Z. L. Wang, Triboelectric nanogenerators as new energy technology and self-powered sensors – principles, problems and perspectives, Faraday Discuss. 176 (2014) 447–458.

[34] Z. L. Wang, J. Chen, L. Lin, Progress in triboelectric nanogenerators as a new energy technology and self-powered sensors, Energy Environ. Sci. 8 (2015) 2250.

[35] J. L. Armitage, A. Ghanbarzadeh, C. Wang, A. Neville, An investigation into the influence of tribological parameters on the operation of sliding triboelectric nanogenerators, Tribology International 155 (2021) 106778.

[36] J. L. Armitage, A. Ghanbarzadeh, M. G. Bryant, A. Neville, Investigating the influence of friction and material wear on triboelectric charge transfer in metal–polymer contacts, Tribology Letters 70:46 (2022).

[37] R. D. I. G. Dharmasena, K. D. G. I. Jayawardena, C. A. Mills, J. H. B. Deane, J. V. Anguita, R. A. Dorey, S. R. P. Silva, Triboelectric nanogenerators: providing a fundamental framework, Energy Environ. Sci., 2017,10, 1801-1811.

[38] R. D. I. G. Dharmasena, S. R. P. Silva, Towards optimized triboelectric nanogenerators, Nano Energy 62 (2019) 530–549.

[39] S. Niu, Y. S. Zhou, S. Wang, Y. Liu, L. Lin, Y. Bando, Z. L. Wang, Simulation method for optimizing the performance of an integrated triboelectric nanogenerator energy harvesting system, Nano Energy 8 (2014) 150–156.

[40] A. G. P. Kottapalli, K. Tao, D. Sengupta, M. S. Triantafyllou, Self-Powered and Soft Polymer MEMS/NEMS Devices, Springer Briefs in Applied Sciences and Technology, 2019.

[41] L. Dhakar, Triboelectric Devices for Power Generation and Self-Powered Sensing Applications, doi 10.1007/978-981-10-3815-0 Edition, Springer Nature Singapore Pte Ltd., 2017.

[42] M. Han, X. Zhang, H. Zhang (Eds.), Flexible and Stretchable Triboelectric Nanogenerator Devices - Toward Self-powered Systems, 2019 Wiley-VCH Verlag GmbH & Co. KGaA, Boschstr. 12, 69469 Weinheim, Germany, 2019.

[43] N. Zhang, C. Tao, X. Fan, Progress in triboelectric nanogenerators as self-powered smart sensors, J. Mater. Res., 32 (9) (2017) 1628–1646.

[44] F. Xi, Y. Pang, W. Li, T. Jiang, L. Zhang, T. Guo, G. Liu, C. Zhang, Z. L. Wang, Universal power management strategy for triboelectric nanogenerator, Nano Energy 37 (2017) 168–176.

[45] M. Alhawari, B. Mohammad, H. Saleh, M. Ismail, Energy Harvesting for Self-Powered Wearable Devices, Springer International Publishing AG, 2018.

[46] B. Ghatak, S. Banerjee, S. B. Ali, R. Bandyopadhyay, N. Das, D. Mandal, B. Tudu, Design of a self-powered triboelectric face mask, Nano Energy 79 (2021) 105387.

[47] F. Wen, Z. Sun, T. He, Q. Shi, M. Zhu, Z. Zhang, L. Li, T. Zhang, C. Lee, Machine learning glove using self-powered conductive superhydrophobic triboelectric textile for gesture recognition in vr/ar applications, Adv. Sci. (2020) 2000261.

[48] R. D. I. G. Dharmasena, J. H. B. Deane, S. R. P. Silva, Nature of power generation and output optimization criteria for triboelectric nanogenerators, Adv. Energy Mater. (2018) 1802190.

[49] H. Zhang, Modeling, simulation, and optimization of miniature triboelectret kinetic energy harvesters, Ph.D. thesis (2019, Université Paris-Saclay, 2019. English. NNT: 2019 SACLC100. tel-02492193).

[50] J. Li, C. Wu, I. Dharmasena, X. Ni, Z. Wang, H. Shen, S.-L. Huang, W. Ding, Triboelectric nanogenerators enabled internet of things: A survey, Intelligent and Converged Networks A 1 (2) (2020) 115–141.

[51] W. Xu, X. Zhou, C. Hao, H. Zheng, Y. Liu, X. Yan, Z. Yang, M. Leung, X. C. Zeng, R. X. Xu, Z. Wang, Slips-teng: robust triboelectric nanogenerator with optical and charge transparency using a slippery interface, National Science Review 6 (2019) 540–550, doi: 10.1093/nsr/nwz025.

[52] S. Wang, L. Lin, Y. Xie, Q. Jing, S. Niu, Z. L. Wang, Sliding-triboelectric nanogenerators based on in-plane charge-separation mechanism, NanoLetters 13 (2013) 2226–2233.

[53] S. Niu, Y. Liu, S. Wang, L. Lin, Y. Zhou, Y. Hu, Z. L. Wang, Theory of sliding-mode triboelectric nanogenerators, Adv. Mater. 25 (2013) 6184–6193.

[54] Y. Lee, S. G. Kang, J. Jeong, Sliding triboelectric nanogenerator with staggered electrodes, Nano Energy 86 (2021) 106062.

[55] G. Brocard, The LTspice XVII Simulator, Commands and Applications, WÜRTH ELEKTRONIK, 2022.

[56] Y. F. Liu, J. Li, Z. M. Zhang, X. H. Hu, W. J. Zhang, Experimental comparison of five friction models on the same test-bed of the micro stick-slip motion system, Mech. Sci. 6 (2015) 15–28.

[57] E. Pennestri, V. Rossi, P. Salvini, P. P. Valentini, Review and comparison of dry friction force models, Nonlinear Dyn 83 (2016) 1785–1801.

[58] M. T. Bengisu, A. Akay, Stick–slip oscillations: Dynamics of friction and surface roughness, J. Acoust. Soc. Am. 105 (1) (1999) 194.

[59] T. Putelat, J. H. P. Dawes, J. R. Willis, Regimes of frictional sliding of a spring–block system, Journal of the Mechanics and Physics of Solids 58 (2010) 27–53.

[60] A. Malthe-Sorenssen, Elementary Mechanics Using Matlab, doi 10.1007/978-3-319-19587-2 Edition, Springer Cham Heidelberg New York Dordrecht London, 2015.

[61] P. Berthoud, T. Baumberger, Shear stiffness of a solid-solid multicontact interface, Proc. R. Soc. Lond. A 454 (1998) 1615–1634.

[62] A. D. Berman, W. A. Ducker, J. N. Israelachvili, Origin and characterization of different stick-slip friction mechanisms, Langmuir 12 (1996) 4559–4563.

[63] P. Stempflé, A. Domatti, J. Takadoum, A. Fahs, P. Carriere, Thermal-controlled frictional behaviour of nanopatterned self-assembled monolayers as triboactive surfaces, Tribology Letters 68 (55) (2020).

[64] J. W. Eaton, D. Bateman, S. Hauberg, R. Wehbring, Octave version 6.4.0, Octave version 6.4.0, 2021.

[65] J. J. Thomsen, A. Fidlin, Analytical approximations for stick-slip vibration amplitudes, International Journal of Non-linear Mechanics 38 (3) (2003) 389–403.

[66] Y. Kligerman, M. Varenberg, Elimination od stick-slip motion in sliding of split or rough surface, Tribology Letters 53 (2014) 395–399.

[67] Z. Yang, H. P. Zhang, M. Marder, Dynamics of static friction between steel and silicon, PNAS 105 (36) (2008) 13264–268.

[68] B. N. J. Persson, V. L. Popov, On the origin of the transition from slip to stick, Solid State Communications 114 (2000) 261–266.

[69] J. Uradnicek, P. Krauss, M. Musil, M. Bachraty, Modeling of frictional stick slip effect leading to disk brake moise vibration and harshness, Proceedings of 23rd International Conference ENGINEERING MECHANICS 2017, Svratka, Czech Republic (2017) 1002–1005.

[70] L. Burstein, MATLAB with Applications in Mechanics and Tribology, IGI Global, 2021.

[71] B. N. J. Persson, M. Scaraggi, A. I. Volokitin, M. K. Chaudhury, et al., Contact electrification and the work of adhesion, EPL 103 (2013) 36003.

[72] W. Y. Yang, J. Kim, K. W. Park, D. Baek, S. Lim, J. Joung, S. Park, H. L. Lee, W. J. Choi, T. Im, Electronic Circuits with MATLAB, PSpice, and Smith Chart, John Wiley & Sons, Inc., 2020.

[73] I. G. Goryacheva, Mechanics of discrete contact, Tribology International 39 (2006) 381–386.

[74] J. Martinez-Vega (Ed.), Dielectric Materials for Electrical Engineering, ISTE Ltd, 2010.

[75] O. Gallot-Lavallée, Dielectric Materials and Electrostatics, ISTE Ltd, 2013.

[76] K. Tian, N. N. Gosvami, D. L. Goldsby, R. W. Carpick, Stick-slip instabilities for interfacial chemical bond-induced friction at the nanoscale, J. Phys. Chem. B (2017).

[77] C. Gao, D. Kuhlmann-Wilsdorf, D. D. Makel, Fundamentals of stick-slip, Wear 162-164 (1993) 1139–1149.

[78] M. Patrascu, S. Stramigioli, Modeling and simulating the stick-slip motion of the microwalker, a mems-based device for microspam, Microsyst Technol 13 (2007) 181–188.

[79] J. S. Park, S. M. Lee, B. S. Joo, H. Jang, The effect of material properties on the stick-slip behavior of polymers: A case study with pmma, pc, ptfe, pvc, Wear 378-379 (2017) 11–16.

[80] K. Nakano, S. Maegawa, Stick-slip in sliding systems with tangential contact compliance, Tribology International 42 (2009) 1771–1780.

[81] M. X. Cohen, Fundamentals of Time-Frequency Analyses in Matlab/Octave, sinc(x) Press, 2014.

[82] C. S. Burrus, M. Frigo, S. G. Johnson, M. Pueschel, I. Selesnick, Fast Fourier Transforms, Rice University, Houston, Texas, http://tftb.nongnu.org/, 2012.

[83] F. Hlawatsch, F. Auger, Time-Frequency Analysis, Wiley-ISTE, 2013.

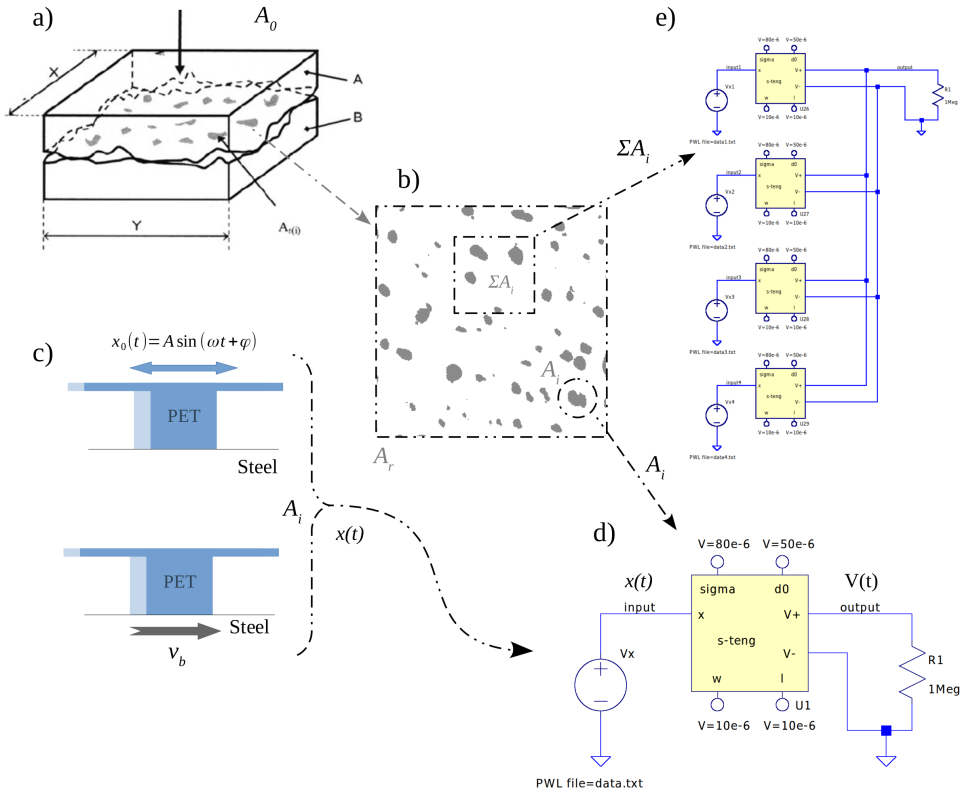

Figure 1: a) Construction of triboelectrical models from the description of a classical tribocontact: a) Difference between the *apparent* (A_0) and the *real* contact area (A_r) owing to their surface roughness; b) Top view of a *real* contact area (A_r), which is actually constituted of numerous *elemental* contact spots (A_i); c) *Elemental* tribological models displaying a single polyethylen (PET) micro-asperity coated by an electrode rubbing on a steel plane for two different kinematic conditions – *ie*, (top) a sinusoidal motion, and (bottom) a continuous sliding motion operating at constant velocity v_b ; d) *Elemental* triboelectrical LTspice component (s-teng) computing the triboelectrical voltage generated during the micro-asperiy sliding ; input of the triboelectrical model is the *real* displacement $x(t)$ of the asperity computed by tribological simulations, described in Fig 1c); e) *Multi-asperity* LTspice triboelectrical model built by wiring many *elemental* triboelectrical models in parallel; it provides the whole triboelectrical signal generated by interactions of asperities constituting the *real* contact area.

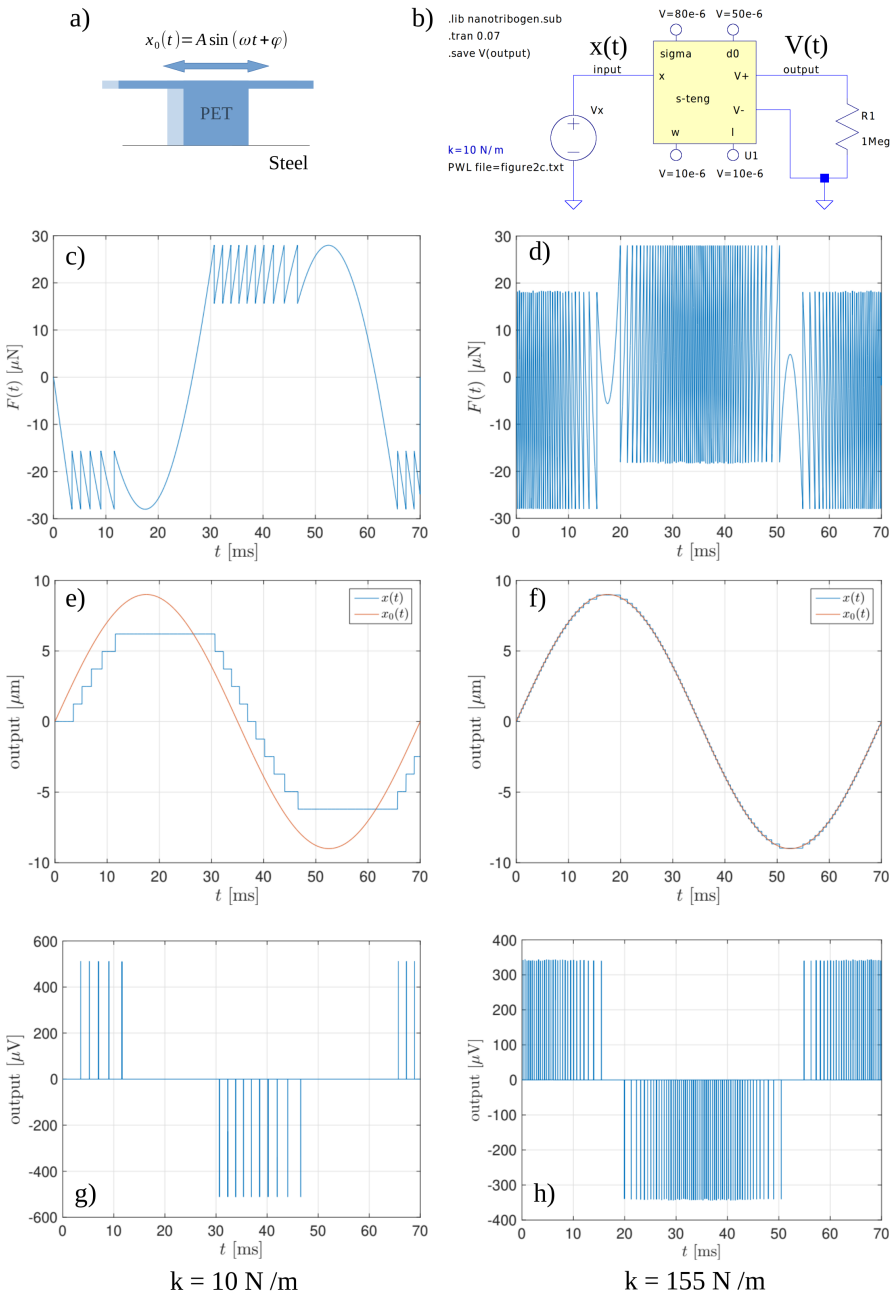

Figure 2: Tribological and triboelectrical simulations of Model 1 computed for two PET stiffnesses – *ie*, 10 N/m and 155 N/m : a) Model 1: a PET micro-asperity is submitted to a sinusoidal motion rubbing on a steel plane in dry friction (see parameters in Table 1); b) *Elemental* triboelectrical model (S-TENG) with parameters reported in Table 2; c) and d) Friction force *vs.* time computed for asperity's stiffness of 10 N/m and 155 N/m, respectively; e) and f) *imposed* (red) and *actual* (blue) displacements of PET micro-asperity *vs.* time for asperity's stiffness of 10 N/m and 155 N/m, respectively; g) and h) voltage output *vs.* time computed by using the S-TENG component for asperity's stiffness of 10 N/m and 155 N/m, respectively.

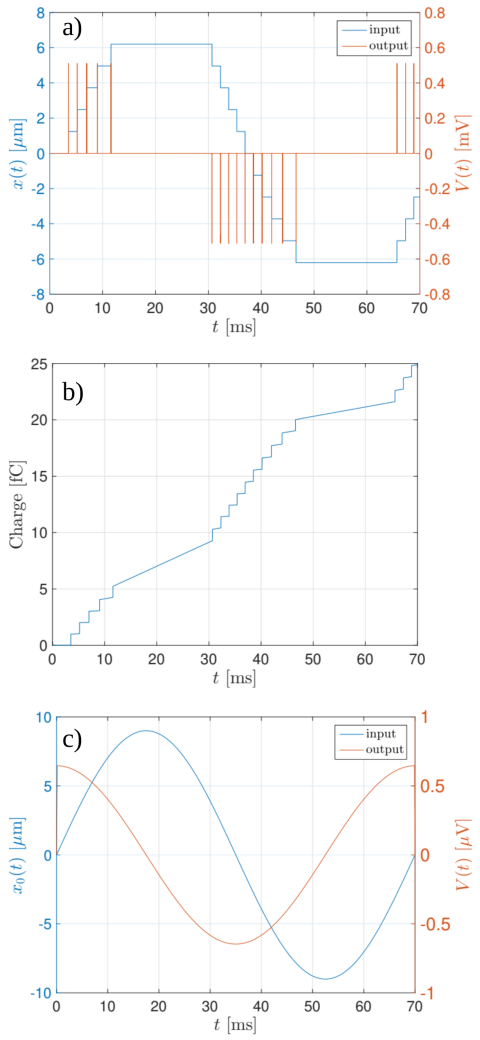

Figure 3: a) Superposition of the triboelectric voltage output $V(t)$ and the *actual* displacement $x(t)$ *vs.* time for an asperity stiffness of 10 N/m; b) Integration of the current flowing out the circuit revealing the charging process in a capacitor or a battery ; c) Superposition of the triboelectric voltage output $V(t)$ and the *imposed* sinusoidal displacement $x_0(t)$ *vs.* time revealing that the triboelectrical output is the derivative of the displacement input signal, and so, the *in situ* assessment of the *elemental* micro-asperity velocity.

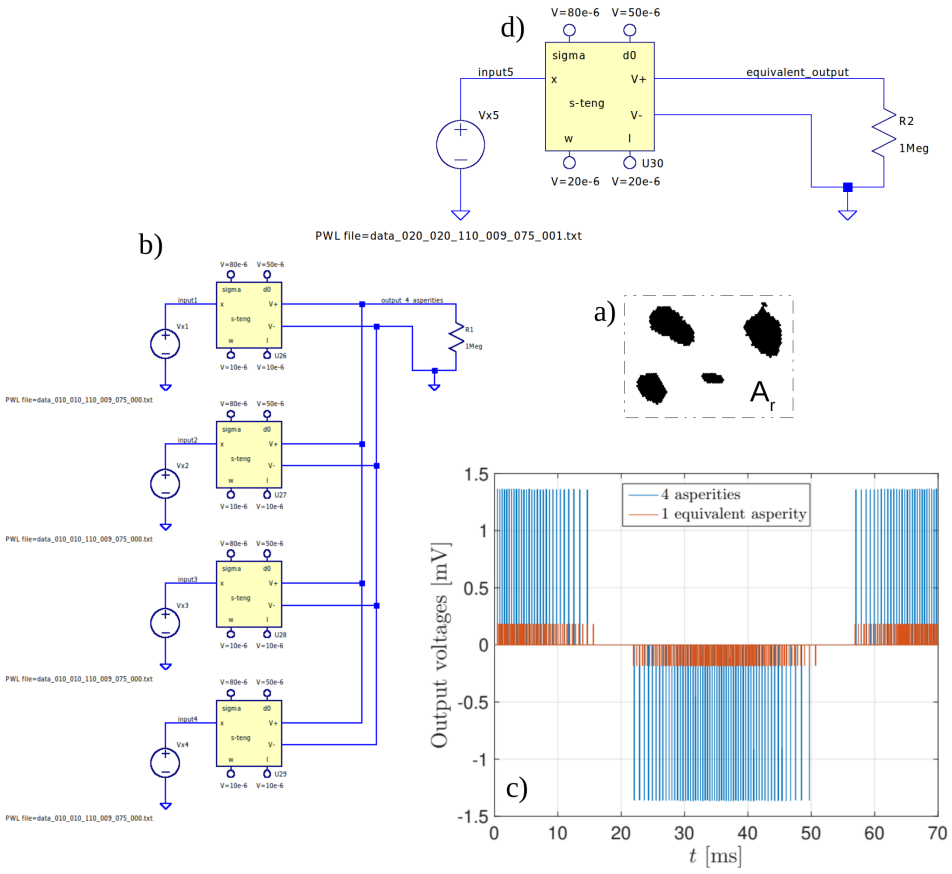

Figure 4: Triboelectrical simulations of a *real* contact area (a) constituted of four micro-asperities in parallel (b). Each asperity suffers tribological behavior of Model 1 and displays the same stiffness of 75 N/m ; c) Triboelectrical voltage *vs.* time of multiple asperities (blue) compared to the one of a single asperity (red) displaying same contact area (d).

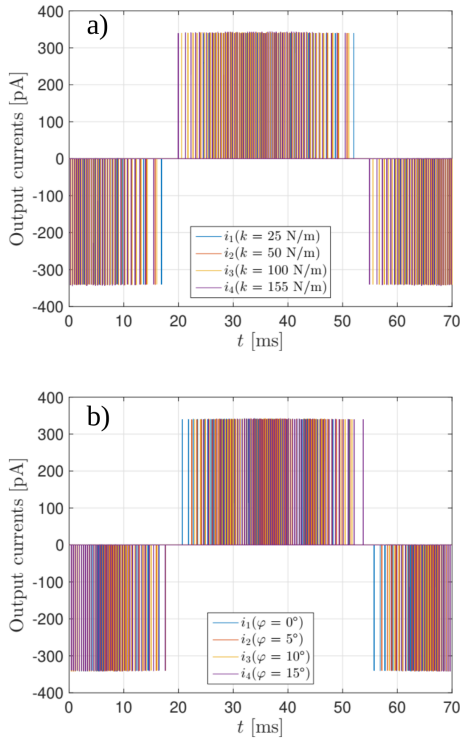

Figure 5: Triboelectrical simulations of a *real* contact area constituted of four micro-asperities in parallel, as shown in Fig. 4b, but displaying specific stiffness of 25, 50, 100 and 155 N/m, respectively: a) Output currents $i_n(t)$ of each triboelectric component plotted *vs.* time (a specific color per asperity stiffness k) ; b) Same results obtained by dephasing all input displacements $x_n(t)$ while stiffness is keeped the same for all asperities (a specific color per phase φ). (NB: LTspice sign convention is that all current flow into a component)

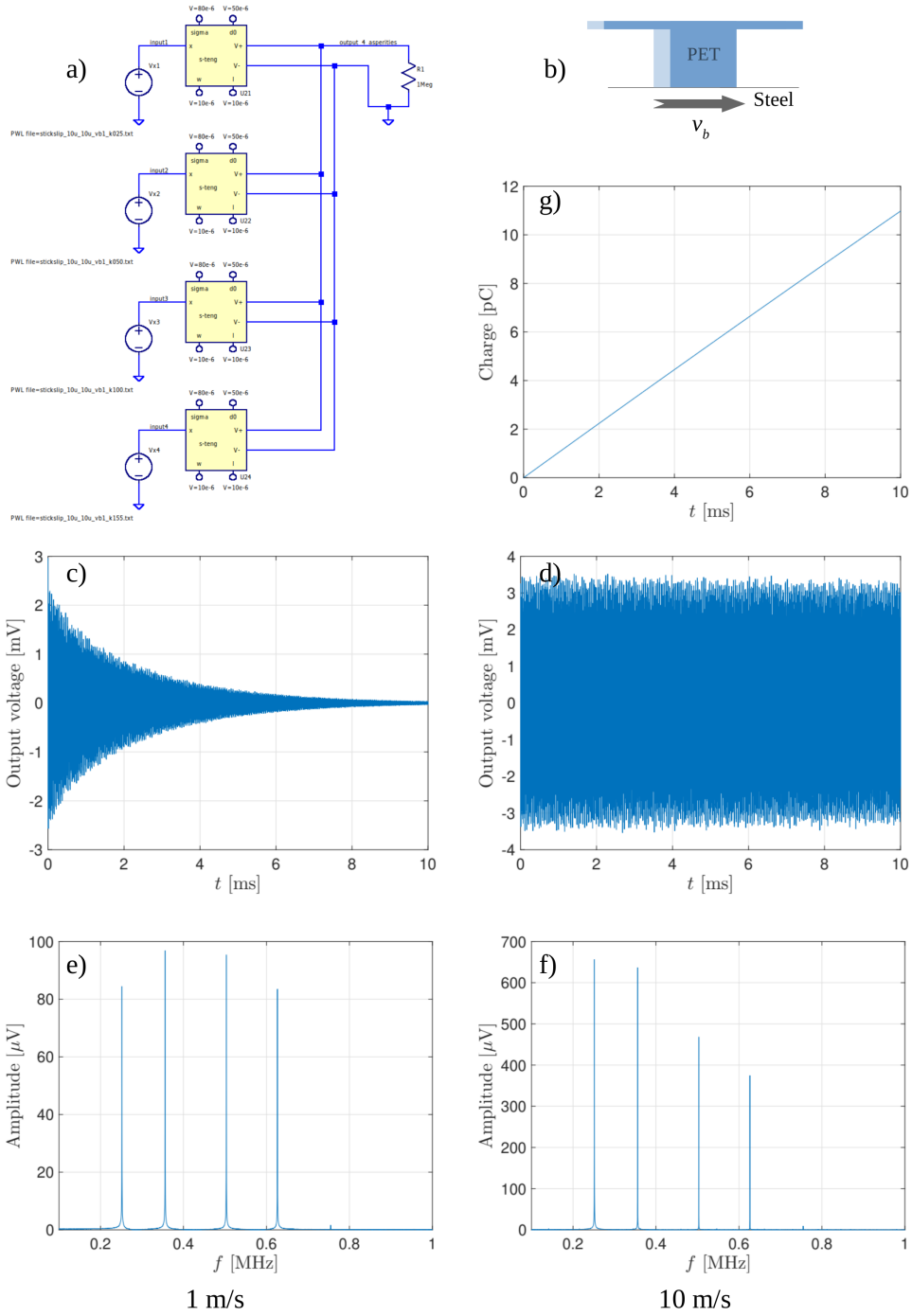

Figure 6: a) Triboelectrical simulations of a *real* contact area constituted of four micro-asperities in parallel, where each asperity follows the tribological Model 2 (b) and displays a specific stiffness ranged from 25 N/m to 155 N/m (Simulation parameters are reported in Table 1) ; c) and d) Triboelectrical voltage *vs.* time of multiple asperities for a steel plane velocity of 1 m/s and 10 m/s, respectively; e) and f) Fast Fourier Transform of the signals plotted in c) and d), respectively; g) Integration of the electric current flowing out the circuit revealing the charging process in a capacitor or battery.

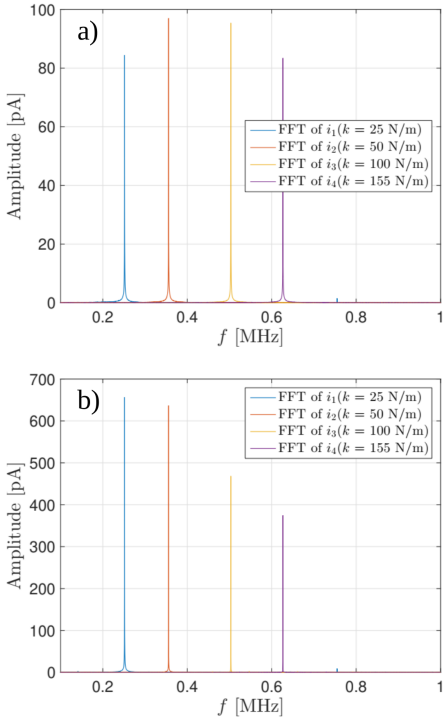

Figure 7: Fast Fourier Transform of the electric currents flowing out each *elemental* triboelectrical component for two drive plane velocities : a) $v_b = 1m/s$ and b) $v_b = 10m/s$, respectively. Peak position in frequency is clearly connected to the asperity's stiffness.

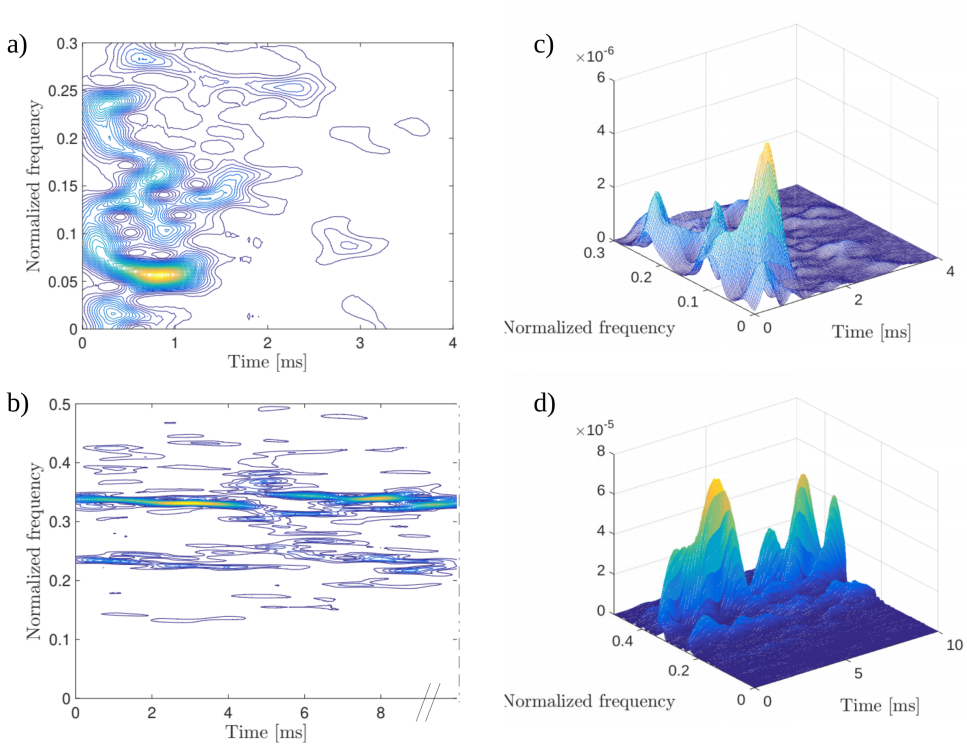

Figure 8: a) and b) Spectrograms of the triboelectrical voltage plotted in Fig. 6c and 6d, respectively; c) and d) their 3D representations.

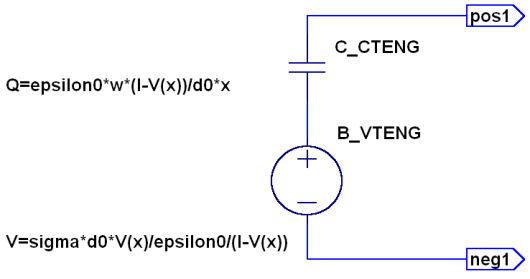

Figure 9: First model of S-TENG.

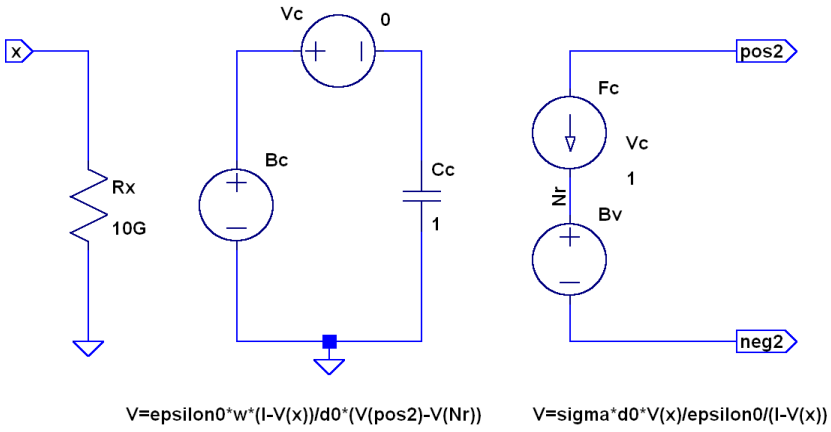

Figure 10: Second model of S-TENG.

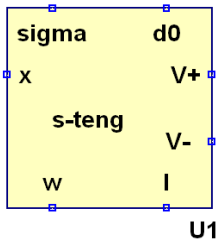

Figure 11: Macro-component of a S-TENG.

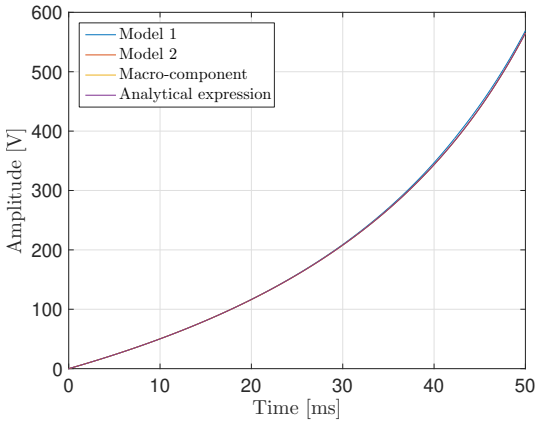

Figure 12: Comparisons of LTspice outputs and analytical equation.